Contents lists available at ScienceDirect

Sensors and Actuators: B. Chemical

Single-trigger dual-modal nanoplatform for in situ switch on cancer diagnosis imaging

Yibing Liu [a], Xue Jiang [b], Wei Wang [a], Wei Zhang [a], Pinyi Ma [a,*], Yibing Huang [b,*], Daqian Song [a,*]

[a] College of Chemistry, Jilin Province Research Center for Engineering and Technology of Spectral Analytical Instruments, Jilin University, Qianjin Street 2699, Changchun 130012, China
[b] Key Laboratory for Molecular Enzymology and Engineering of the Ministry of Education, School of Life Sciences, Jilin University, Qianjin Street 2699, Changchun 130012, China

ARTICLE INFO

ABSTRACT

Tumor markers in situ switch on nanoplatform is of great significance for disease early diagnosis and accurate treatment. It has significant advantages to realize simultaneous detection of multiple signals through single signal triggering. However, traditional nanoplatform often needs complex modification and integration of multiple materials. Herein, to achieve "one stone for two birds" and simplify nanoplatform structure, a dual-modal system was developed for glutathione (GSH)-triggered in situ switch on imaging of cancer. The transition metal oxide FeOOH shell was generated around CuInZnS quantum dots (CIZS QDs), and the near-infrared (NIR) fluorescence of QDs could be quenched. After being reduced to Fe^{2+} by GSH which normally overexpressed in cancer cells, CIZS QDs with fluorescence will generate. Therefore, the GSH-triggered fluorescence recovery could be used for in situ switch on cancer diagnostic imaging of cells and tumor-bearing mice. Furthermore, the reaction product Fe^{2+} enabled followed chemodynamic therapy (CDT) and magnetic resonance (MR) imaging properties to realize dual-modal diagnosis imaging. Compared with other FeOOH nanostructures, our method was more simple and efficient. Hence, this study provided a new attempt to construct versatile nanoplatform, which integrated cancer diagnosis imaging capability and may be applied in subsequent therapeutics.

1. Introduction

Cancer has always been one of the major threats to human life and health, and human has been looking for ways to diagnose and treat cancer [1–3]. Timely diagnosis and accurate positioning of tumor are the key to successful treatment [4,5]. Currently, various imaging techniques are used to achieve tumor diagnosis in clinical practice [6–9]. Among them, in situ imaging is an effective method to obtain accurate position information of target analytes [10,11]. When the probe is specifically activated by the target analyte, it releases signal molecules to achieve real-time in situ imaging of the analyte [12,13]. In situ imaging through magnetic resonance (MR) and fluorescence technology are two important ways [14–17]. Near-infrared (NIR) fluorescence imaging has excellent anti-biological interference performance and is suitable for preclinical qualitative analyses [18,19]. However, applications of fluorescence imaging are limited by its poor tissue permeability

[20]. MR imaging is a classic clinical imaging technique that has high spatial resolution and high tissue penetration [21,22]. Thus, it can overcome the shortcoming of fluorescence imaging well. Integrating multi-modal imaging techniques into one system could improve the efficiency of diagnostic imaging [23,24].

Glutathione (GSH), as an important cellular reducing agent, is overexpressed in tumor cells [25,26]. Due to its much lower content in normal cells, GSH-responsive probe can be utilized to differentiate cancer and normal cells or employed in early cancer diagnosis [27,28]. There have been many studies devoted to the detection of GSH, which is owing to its important role in biological processes [29–31]. Furthermore, it is of great significance to construct an in situ imaging probe using GSH as the activation tool to realize tumor site specific imaging. Quaternary Cu-In-Zn-S (CIZS) semiconductor quantum dots (QDs) are derived from traditional ternary I−III−VI QDs [32]. The incorporation of Zn^{2+} could greatly enhance their photoluminescence (PL) efficiency
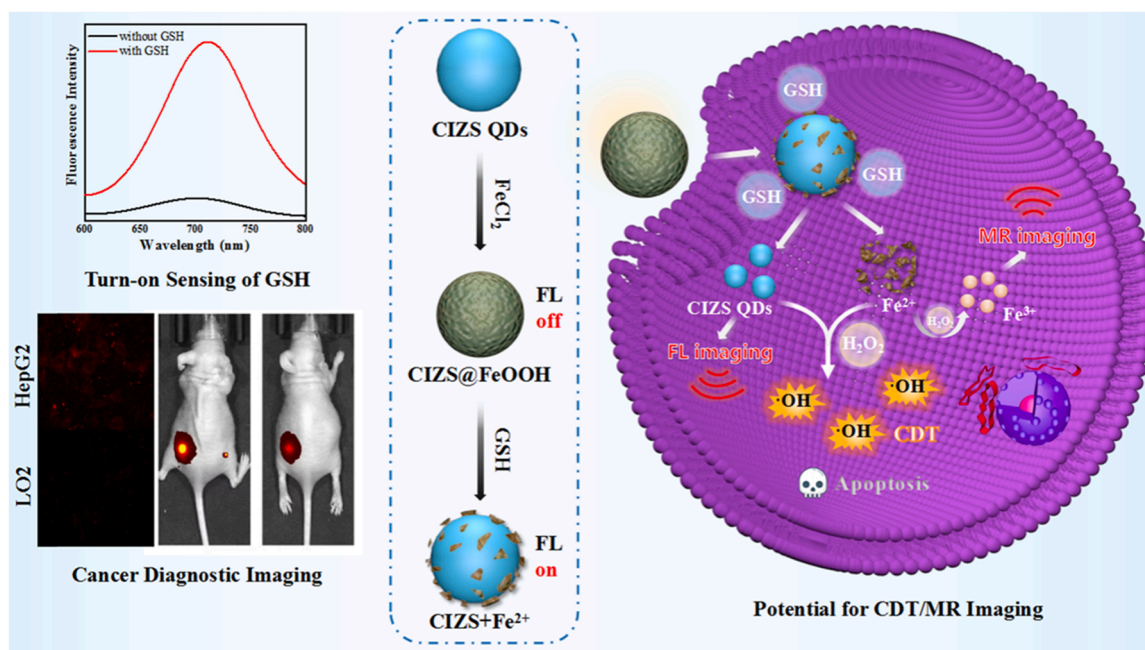
Scheme 1. Schematic illustration of the smart system based on CIZS@FeOOH.
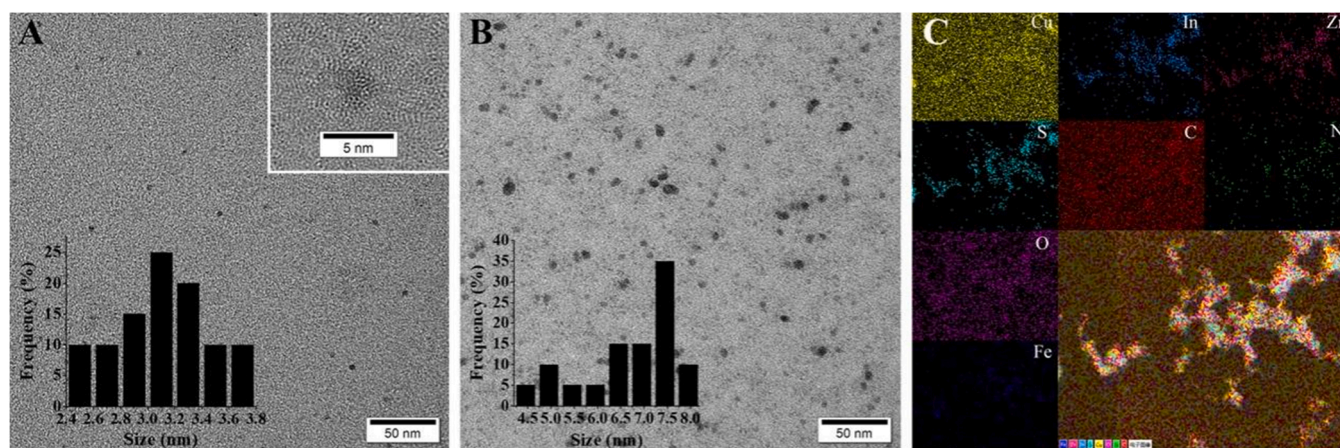

Fig. 1. TEM images and size distribution histograms (inset) of (A) CIZS QDs and (B) CIZS@FeOOH. (C) Elemental mapping of CIZS@FeOOH.

[33]. CIZS QDs without toxic element cover a broad tunable emission range from visible to near-infrared (NIR) region, which could serve as a contrast agent for cell imaging and in *vivo* NIR fluorescence imaging [34]. Iron oxyhydroxide (FeOOH) has a wide range of applications, several studies also focused on the fluorescence quenching ability of FeOOH with different morphologies [35,36]. As an efficient fluorescence quencher, FeOOH can effectively quench the fluorescence of nanomaterials, and can be degraded to Fe^{2+} by GSH to restore fluorescence. Compared with the fabrication of FeOOH nanosheets, our method is fairly simple and no significant increase in QDs size is observed, which maintains the good cell penetration of QDs. Therefore, making it more suitable for intracellular GSH imaging and cancer diagnostic imaging. Moreover, the reaction product Fe^{2+} also enables subsequent MR imaging and therapy functions.

In this work, in order to solve the shortcomings of traditional nanoplatform that is complex to modify and needs to integrate multiple materials into one system, we designed a simple and efficient CIZS@FeOOH nanoplatform for in situ activated cancer diagnostic imaging in *vitro* and in *vivo*. The platform could induce different imaging signals with single trigger GSH and had additional therapeutic benefits.

Transition metal oxide shell FeOOH was generated around CIZS QDs to quench their near-infrared (NIR) fluorescence. After being decomposed into Fe^{2+} under the stimulation of GSH, the fluorescence was recovered. Thus, a GSH-responsive modulation for in situ switch on imaging of cancer cells and tumor-bearing mice was constructed. Apart from the sensing and imaging ability of the system, we also briefly discussed its chemodynamic therapy (CDT) property and followed magnetic resonance (MR) imaging. CIZS QDs which exhibited acid-dependent peroxidase-mimicking catalytic property, could react with H_2O_2 under mildly acidic conditions and generate highly toxic·OH. The reaction product Fe^{2+}-triggered Fenton reaction acted as another high-performance catalytic agent that contributed to the synergistic effect of CDT. The generation of Fe^{3+} from the Fenton reaction enabled activatable T_1-weighted MR imaging to achieve pretreatment guidance and Fenton reaction monitoring. Overall, CIZS@FeOOH nanoplatform not only has good performance for in situ switch on cancer diagnosis imaging, but also shows the potential for nanomedicine and subsequent diagnostics (Scheme 1). This study provides a valuable guideline for designing new nano-theranostic system.
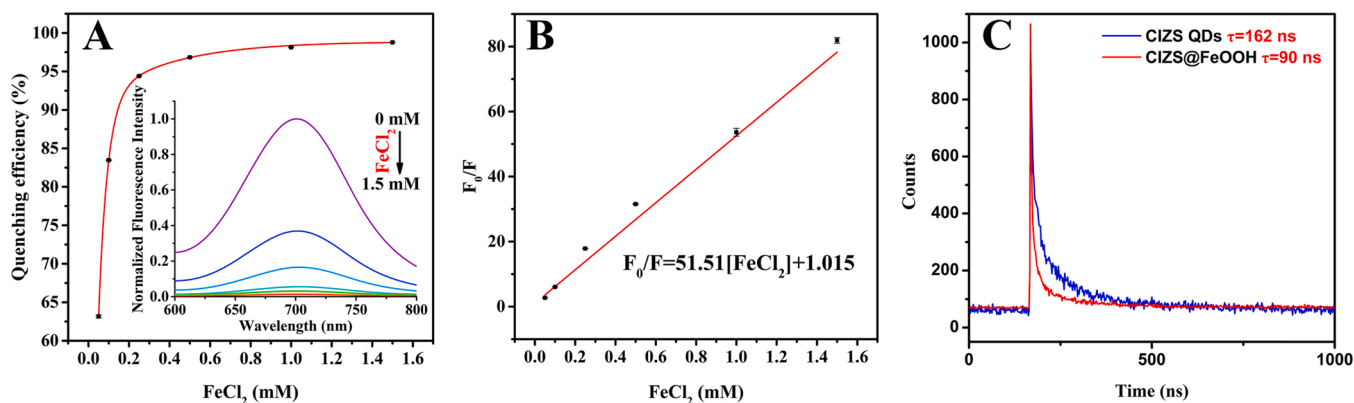
Fig. 2. . (A) Dependency of fluorescent quenching efficiency on FeCl$_2$ concentration. (B) The relationship between F$_0$/F and FeCl$_2$ concentration. F$_0$ and F stand for the fluorescence intensity of CIZS QDs and CIZS@FeOOH. (C) Fluorescence lifetime curves of CIZS QDs and CIZS@FeOOH.
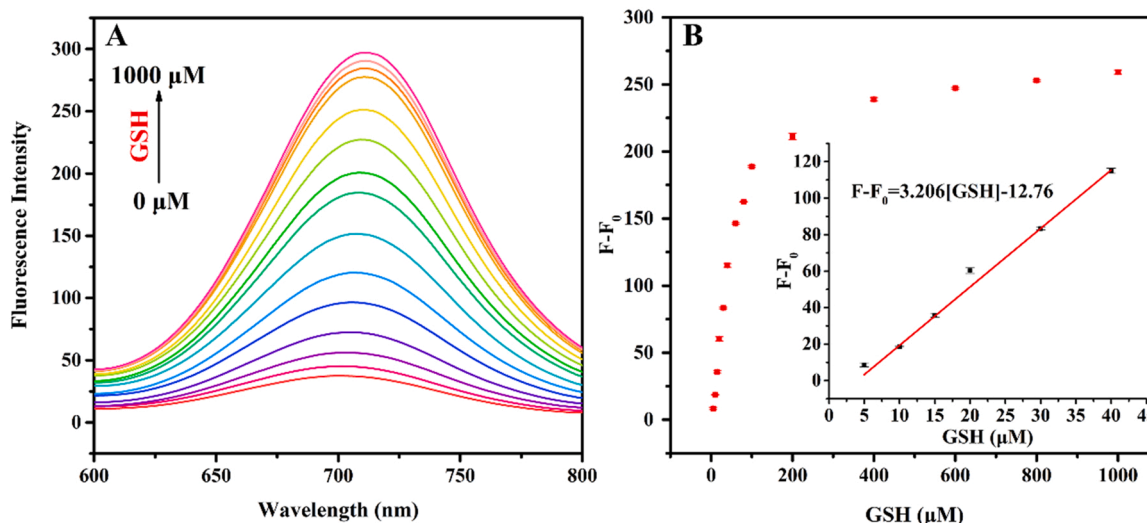

Fig. 3. . (A) Fluorescence spectra of CIZS@FeOOH in the presence of GSH at different concentrations. (B) Linear relationship between F-F$_0$ and GSH concentration (F$_0$/F: the fluorescence intensity before/after the addition of GSH).

2. Experimental section

2.1. Synthesis of CIZS QDs and CIZS@FeOOH

CIZS QDs were synthesized according to a previous method with minor modifications [33]. Typically, CuCl$_2$·2 H$_2$O (0.011 mmol), ZnCl$_2$ (0.0022 mmol), InCl$_3$·4 H$_2$O (0.04 mmol), Na$_2$S·9 H$_2$O (0.066 mmol), sodium citrate dehydrate (0.16 mmol), and GSH (0.133 mmol) were dissolved in 20 mL of ultrapure water in a three-necked flask. The pH of the solution was maintained at about pH 6, and the solution was heated to boiling for 1 h. After cooling down to 80 °C, 0.05 mmol each of ZnCl$_2$, GSH and Na$_2$S·9 H$_2$O were added to the reaction system in the respective order. The solution was further kept at 80 °C for 1 h. After cooling down to room temperature, the solution was precipitated with ethanol and collected by centrifugation at 8000 rpm for 15 min. The obtained CIZS QDs were re-dispersed in water for subsequent use.

In the synthesis of CIZS@FeOOH [37], 1 mL of the prepared CIZS QDs (15 mg mL^{-1}) was mixed with 50 μL of FeCl$_2$ (0.1 M), and the mixture was diluted to 10 mL with ultrapure water. The mixture was stirred vigorously at room temperature for 30 min. Finally, the unreacted metal ions were wiped off by centrifugation and the obtained CIZS@FeOOH was re-dispersed in ultrapure water.

2.2. Fluorescence sensing of GSH by CIZS@FeOOH

To study the fluorescent response of CIZS@FeOOH to GSH, 500 μL of CIZS@FeOOH (1.5 mg mL^{-1}) was mixed with 100 μL of GSH at different concentrations. The mixture was diluted to 1 mL with PBS solution (10 mM, pH 6). After reacting for 10 min at room temperature, the fluorescence spectrum of the mixture was measured at an excitation wavelength of 400 nm.

3. Results and discussion

3.1. Characterization of CIZS@FeOOH

CIZS QDs were synthesized by a one-pot aqueous approach. The TEM image shown in Fig. 1A illustrated that CIZS QDs had an average size of 3.2 nm and good monodispersity. The EDX elemental mapping image indicated that CIZS QDs contained Cu, In, Zn, S, C, N and O elements (Fig. S1). The EDS result (Fig. S2) also revealed the ratio of the composed elements. After ferrous ions were added, the transition metal oxide shell was formed as a result of the metal ions hydrolysis. As shown in the TEM image of CIZS@FeOOH (Fig. 1B), the average particle size increased to 7.5 nm. The EDX elemental mapping image in Fig. 1C indicated the presence of Fe element and that in Fig. S3 revealed the ratio of the elemental components. The Zeta potential of CIZS QDs was − 47 mV,
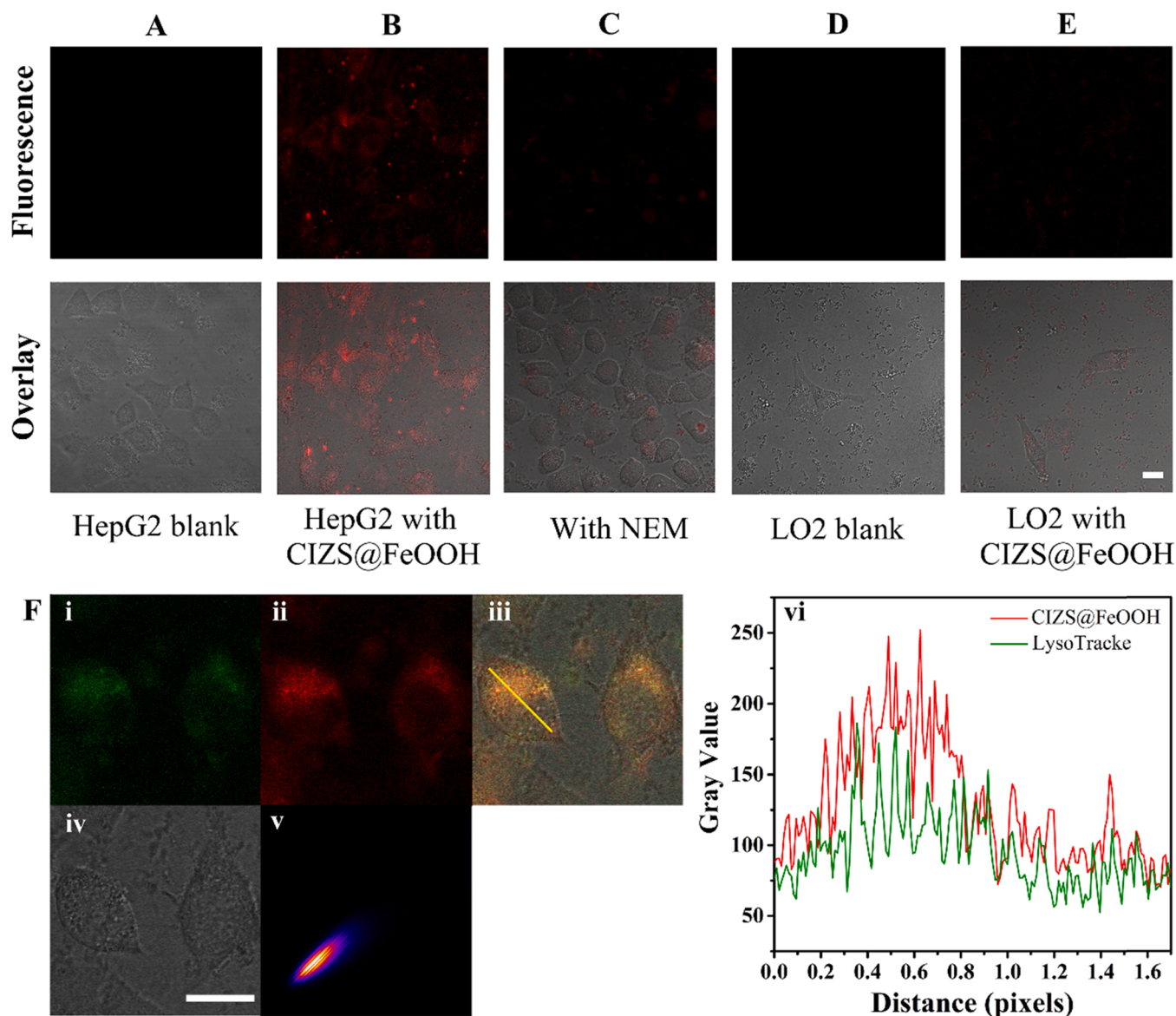
Fig. 4. Confocal fluorescence images of: (A) HepG2 cells only; (B) HepG2 cells incubated with CIZS@FeOOH (1.5 mg mL^{-1}) for 1 h; (C) HepG2 cells pretreated with NEM (500 μM) for 20 min, followed by CIZS@FeOOH (1.5 mg mL^{-1}) for 1 h; (D) LO2 cells only; and (E) LO2 cells incubated with CIZS@FeOOH (1.5 mg mL^{-1}) for 1 h. (F) Co-localization study: (i) green channel of LysoTracker Green; (ii) red channel of CIZS@FeOOH; (iii) overlay of green and red channel; (iv) brightfield image of cells; (v) intensity correlation between CIZS@FeOOH and LysoTracker; and (vi) intensity profile of CIZS@FeOOH and LysoTracker. Scale bar: 50 μm.

and increased to − 21.93 mV after FeOOH coating (Fig. S4A). Moreover, the dynamic light scattering (DLS) data (Fig. S4B) showed the mean size of CIZS QDs increased from 21.04 nm to 78.82 nm, which further confirmed the successful formation of CIZS@FeOOH. The FT-IR spectrum of CIZS QDs was shown in Fig. S5A. The absorption peaks located at 2925 cm^{-1} and 2855 cm^{-1} were attributed to the asymmetric stretching of C-H. The peaks at 1555 cm^{-1} and 1396 cm^{-1} corresponded to the asymmetric and symmetric stretching of −COO$^-$. The disappearance of the –SH vibration observed at 2520 cm^{-1} indicated that the capping agents may bind to the surface of QDs through SH groups [23]. Fig. S5B depicted the FT-IR spectrum of CIZS@FeOOH, showing that there were no obvious changes compared with CIZS QDs. The absorption peak located at 1051 cm^{-1} could be ascribed to the bending vibrations of Fe−O−H in FeOOH [36].

3.2. Quenching mechanism of CIZS@FeOOH

CIZS@FeOOH was synthesized by adding ferrous ions to CIZS QDs under vigorous stirring at room temperature. Due to electrostatic interactions, positively charged metal ions tend to be adsorbed on the surface of negatively charged CIZS QDs, and this results in the formation of a transition metal oxide shell through hydrolysis of the metal ions, causing subsequent precipitation of insoluble substances around CIZS QDs [37]. As the ferrous ion concentration increased, the fluorescence intensity of CIZS QDs gradually decreased until reaching a plateau when the concentration of FeCl$_2$ reached 0.5 μM (Fig. 2 A). Generally, there are two types of fluorescence quenching: dynamic quenching and static quenching. Dynamic quenching is the process in which the interaction between the quencher and the fluorescent molecules at an excited state causes the fluorescence intensity to decrease. Static quenching refers to the process in which the quencher and the fluorescent molecules at a ground state form a non-luminescent complex with reduced fluorescence intensity [35]. Both dynamic quenching and static quenching can theoretically be described by the Stern-Volmer equation: $F_0/F = 1 + K_{SV}C_{FeOOH}$ (where C_{FeOOH} stands for the concentration of the quencher; F_0 and F stand for the fluorescence intensity in the absence
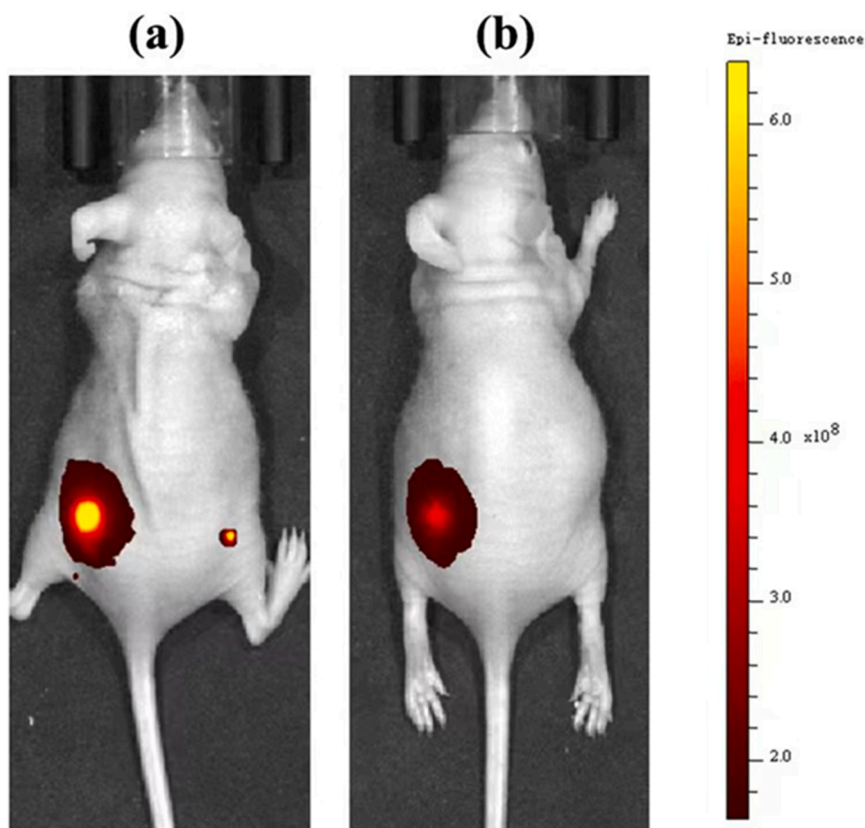
Fig. 5. Fluorescence images of (a) tumor-bearing mice injected with 100 μL CIZS@FeOOH (50 mg mL^{-1}) into tumor (intratumorally) and muscle site (intramuscularly). (b) NEM (2 mM, 30 min)-pretreated tumor-bearing mice injected with 100 μL CIZS@FeOOH (50 mg mL^{-1}) into tumor (intratumorally).

and presence of FeOOH, respectively; and K_{SV} is the Stern−Volmer quenching constant). As shown in Fig. 2B, good linear relationship between F_0/F of CIZS QDs and the concentration of FeCl$_2$ was observed, which proved there was only one quenching mechanism in the quenching process. K_{SV} was calculated to be 51.51 mM^{-1} based on the slope of F_0/F versus [Fe]. To further illustrate the quenching mechanism, the fluorescence lifetimes of CIZS QDs and CIZS@FeOOH were measured. As can be seen in Fig. 2 C, the fluorescence lifetime was significantly reduced, suggesting that the fluorescence quenching of CIZS QDs caused by FeOOH was attributed to dynamic quenching.

3.3. Fluorescence response of CIZS@FeOOH to GSH

With GSH, the FeOOH shell will reacted with reductive substance into the ferrous ions and glutathione disulfide (GSSG), allowing the fluorescence intensity of CIZS QDs to be recovered. Thus, CIZS@FeOOH could be utilized in ultrasensitive detection of GSH. The generation of Fe^{2+} was identified by phenanthroline, as shown in Fig. S6, the absorbance of phenanthroline increased after the introduction of GSH. To find the optimal GSH detection conditions, we studied the influence of several reaction conditions on the performance of the probe. As shown in Fig. S7, the fluorescence intensity gradually increased with time and reached the equilibrium within 10 min, which demonstrated that the reaction occurred at a rapid rate at room temperature. We also investigated the effect of pH. As displayed in Fig. S8, weakly acidic (similar to the microenvironment of tumors and cancer cells) and neutral conditions were more conducive to the progress of the reaction. To investigate the feasibility of using CIZS@FeOOH in GSH sensing, the change of fluorescence with different concentrations of GSH was studied. As shown in Fig. 3 A, the fluorescence intensity increased with the increase of GSH concentration from 5 to 1000 μM. Good liner relationship

between $F-F_0$ and GSH concentrations could be found in the range of 5–40 μM (Fig. 3B) with an r value of 0.9946. The detection limit (LOD) was calculated as 1.50 μM (3σ/k). Compared with other GSH sensing probes listed in Table S1, our probe was highly efficient and comparable. Although the LOD was not the lowest, it was sufficient to detect GSH in human serum and living cells (0.5–10 mM). Too low LOD can also increase the background signal of cancer diagnostic imaging. Furthermore, we compared the variation of fluorescence signal caused by metal ions, amino acids and proteins without and with GSH. As shown in Fig. S9, homocysteine (Hcy) and cysteine (Cys) could also cause slight fluorescence recovery. However, their concentrations are much lower compared with GSH concentrations in biological systems [38]. Especially in cancer cells, GSH concentration is nearly 10 times higher than that in normal cells [39]. Therefore, in the cell environment, the recovery of fluorescence intensity was mainly caused by GSH and the developed probe could be used for in situ imaging of tumor sites. The recovery for the determination of GSH in human serum samples was conducted by standard addition method. As can be seen in Table S2, the recoveries ranged from 97.86% to 101.7%, indicating that the CIZS@FeOOH based assay was reliable and accurate in real samples determination.

3.4. Diagnostic imaging of cancer

To investigate the cancer cell-specific imaging ability of CIZS@FeOOH, confocal images of normal and cancer cells were evaluated. As shown in Fig. 4A-E, after incubating HepG2 cells with CIZS@FeOOH, red fluorescence was observed in the cells. Conversely, nearly no fluorescence was detected in HepG2 cells pre-treated with NEM (thiol-reactive inhibitors). These results suggested that the fluorescence recovery was mainly due to intracellular GSH. Furthermore, we evaluated
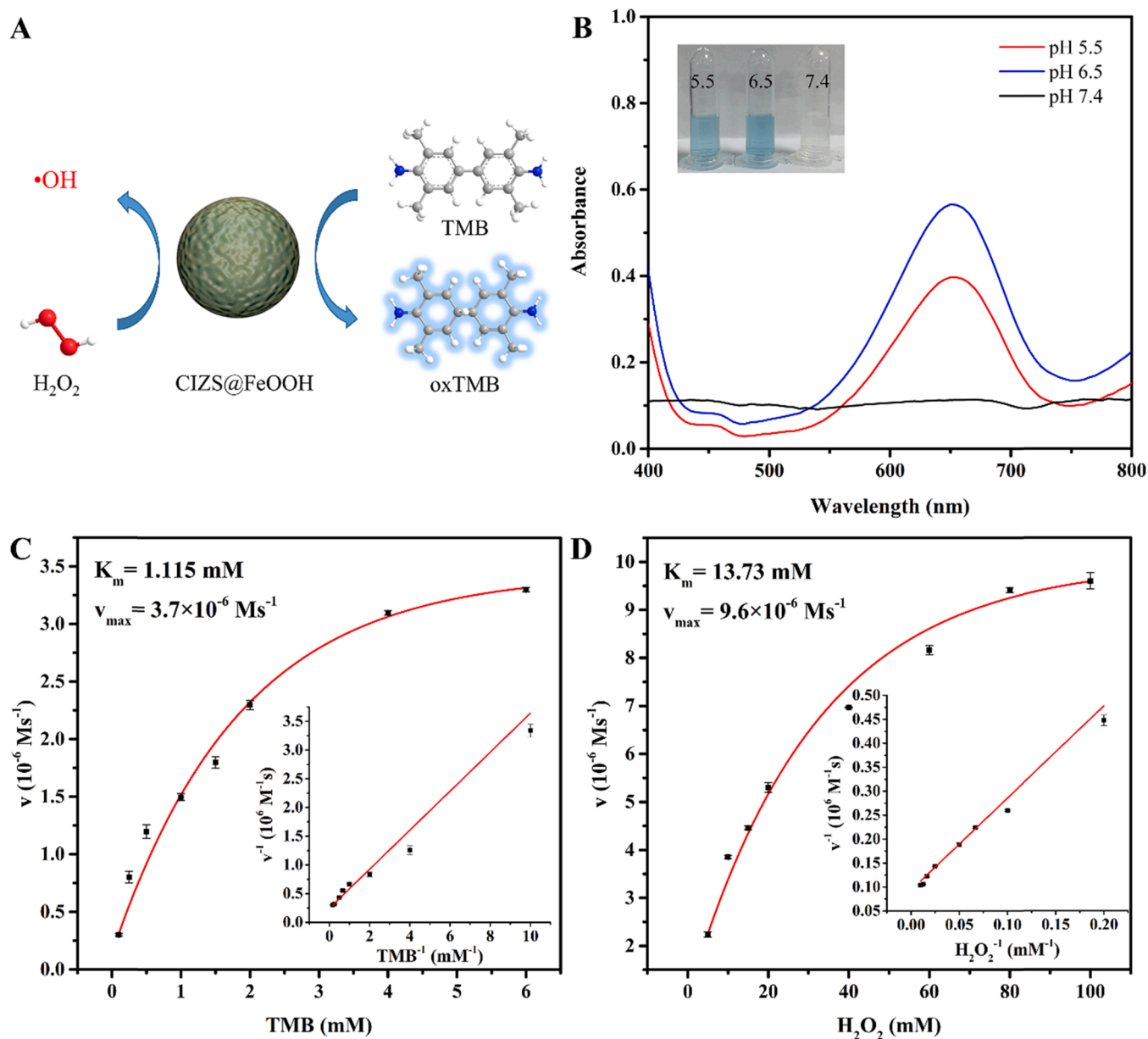
Fig. 6. . (A) Schematic illustration of the catalytic oxidation of TMB. (B) Catalytic oxidation of TMB by CIZS@FeOOH (1.5 mg mL^{-1}) at different pH values. Steady state kinetics of CIZS@FeOOH (1.5 mg mL^{-1}) in the presence of (C) TMB and (D) H$_2$O$_2$ at varying concentrations.
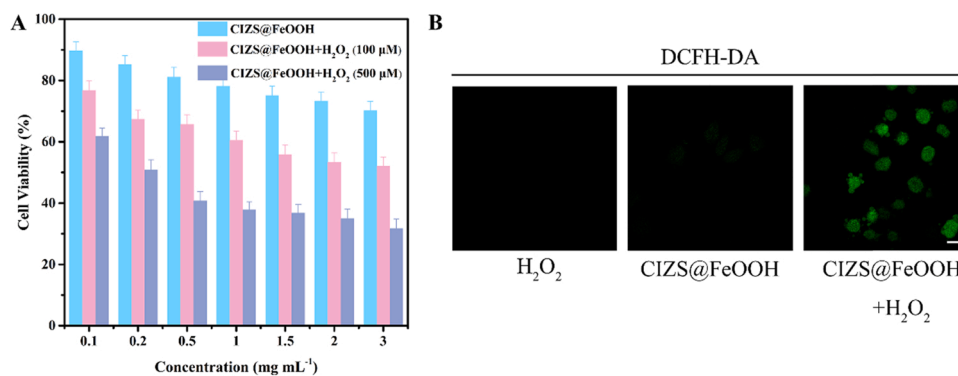

Fig. 7. . (A) Viability of HepG2 cells treated with CIZS@FeOOH (1.5 mg mL^{-1}) and H$_2$O$_2$. (B) Fluorescence images of HepG2 cells stained with DCFH-DA. (CIZS@FeOOH: 1.5 mg mL^{-1}; H$_2$O$_2$: 100 μM) Scale bar: 50 μm.
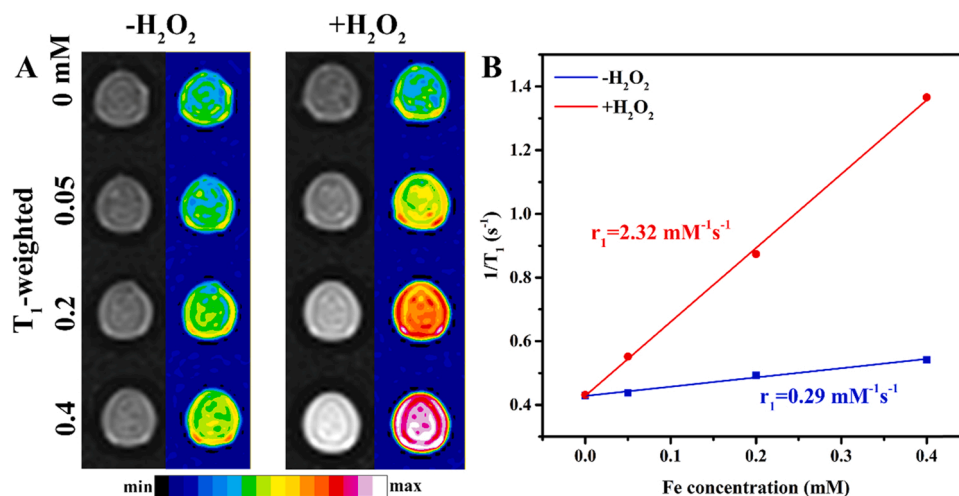
Fig. 8. . (A) T_1-weighted MR images of CIZS@FeOOH at different concentrations in the absence and presence of H_2O_2 (100 μM). (B) Plots of $1/T_1$ versus Fe concentration without and with H_2O_2 (100 μM).

the fluorescence of LO2 cells incubated with CIZS@FeOOH. Extremely week fluorescence was observed, which was due to the low concentration of GSH in normal cells. Therefore, owing to the difference between GSH contents in cancer and normal cells, the probe can be employed in cancer cell-specific imaging.

Co-localization experiments were conducted to explore the localization of CIZS@FeOOH in organelles. The red channel of CIZS@FeOOH overlapped well with the green channel of LysoTracker Green (Fig. 4 F). According to the intensity correlation diagram, the Pearson's correlation coefficient for the lysosome co-localization was calculated to be 0.95. These results demonstrated that lysosome was the terminal target of CIZS@FeOOH.

The GSH-activation of CIZS@FeOOH in *vivo* was explored in HepG2 cell xenograft tumor model. As shown in Fig. 5a, the tumor site exhibited stronger fluorescence compared with the muscle site, demonstrating the higher level of GSH in the liver cancer tumor. After down-regulating GSH level in tumor site by NEM, decreased fluorescence was showed (Fig. 5b). The turn-on fluorescence in *vivo* was consistent with that in solution and in *vitro*, which indicated the feasibility of CIZS@FeOOH in monitoring GSH level in *vivo* and in situ tumor imaging.

3.5. Performance in chemodynamic therapy

The CDT property of the system could be ascribed to two parts: the Cu-based peroxidase-mimicking catalytic property and the GSH-activated Fe^{2+}-triggered Fenton reaction. Firstly, we evaluated the peroxidase-mimicking catalytic activity of CIZS@FeOOH through TMB oxidation reaction. Peroxidase could catalyze the reaction between TMB and H_2O_2 to generate blue oxidized TMB (oxTMB), which has a maximum absorbance at 652 nm (Fig. 6A). By monitoring the absorbance of oxTMB, the peroxidase and peroxidase enzyme-like activities can be confirmed. From Fig. S10, the influence of the environmental pH and temperature on the peroxidase-like activity of CIZS@FeOOH was investigated. It was worth noting that the changes in color and absorbance of oxTMB in CIZS@FeOOH-H_2O_2 system under a mild acidic medium were more obvious compared with those in a neutral medium (Fig. 6B). This showed that the catalytic activity of CIZS@FeOOH exhibited obvious pH dependency, thus could realize CDT in acidic tumor microenvironment without damaging normal tissues. To further evaluate the catalytic ability, steady-state catalytic kinetics was studied. When utilizing TMB as substrate (Fig. 6C), the maximum velocity (V_{max}) and Michaelis−Menten constant (K_m) of CIZS@FeOOH were estimated as 3.7×10^{-6} M s^{-1} and 1.115 mM, respectively. When utilizing H_2O_2 as substrate (Fig. 6D), V_{max} and K_m were estimated as 9.6×10^{-6} M s^{-1}

and 13.73 mM, respectively.

GSH could decompose CIZS@FeOOH into Fe^{2+} and then triggers the Fenton reaction to generate highly toxic·OH. Thus, Fe^{2+} could serve as another CDT agent. To verify the generation of·OH from Fe^{2+}, the degradation of methylene blue (MB) by·OH was assessed. As shown in Fig. S11, after incubating CIZS@FeOOH with H_2O_2 at pH 7.4, the change in absorbance of MB was not apparent. This result was owing to the pH restriction on Cu-based peroxidase-mimicking catalytic performance. However, after treating the system with GSH, MB was effectively degraded by Fe^{2+}-generated·OH. Hence, it appeared that CIZS@FeOOH underwent Cu-based and GSH-activated Fe^{2+}-based synergistic CDT through different catalytic pathways.

Inspired by its unique property, we further investigated the CDT performance of CIZS@FeOOH at the cellular level using HepG2 cells. As shown in Fig. 7A, the cell viability was dependent on the concentrations of H_2O_2 and CIZS@FeOOH, demonstrating that the cell inhibition was triggered by·OH. To further prove the intracellular ROS generation, the fluorescence probe 2′,7′-dichlorodihydrofluorescein diacetate (DCFH-DA) was used. As displayed in Fig. 7B, the group treated with H_2O_2 or CIZS@FeOOH alone showed weak DCF fluorescence. After treated with H_2O_2 plus CIZS@FeOOH, intensive green fluorescence was observed, demonstrating the intracellular ROS generation.

3.6. Performance in MR imaging

High magnetic moment and long electron spin relaxation time of paramagnetic Fe^{3+} ions can shorten the T_1 relaxation time of surrounding water protons, allowing Fe^{3+} to serve as an activatable T_1 MR imaging contrast agent [40]. GSH could reduce CIZS@FeOOH to form ferrous ions, and the subsequent Fenton reaction could then induce the transition of iron valence from Fe^{2+} to Fe^{3+}. Thus, CIZS@FeOOH showed great potential to be applied in activated T_1-weighted MR imaging and Fenton reaction monitoring. We evaluated the T_1 MR imaging performance of different concentrations CIZS@FeOOH. As shown in Fig. 8 A, after incubation with GSH, the T_1-weighted MR imaging signal was not significantly changed, which was indicative of divalent iron valence. Additionally, the longitudinal relaxivity r_1 was calculated to be 0.29 mM^{-1} s^{-1}. After the addition of H_2O_2, the T_1-weighted MR imaging signal increased and showed a dependence on the dose of CIZS@FeOOH. The longitudinal relaxivity r_1 increased to 2.32 mM^{-1} s^{-1}, indicating a greatly enhanced T_1 relaxation (Fig. 8B). The T_1 MR imaging signal resulted from Fe^{3+} was indicative of effective Fenton reaction-induced transition of iron valence from Fe^{2+} to Fe^{3+}. Based on the above results, CIZS@FeOOH could serve as a GSH-Fenton reaction-triggered

activatable T_1 MR imaging contrast agent.

4. Conclusion

In conclusion, a nanoplatform with single trigger induction of dual-modal signals and theranostic function was constructed. The reduction of FeOOH shell triggered by GSH could induce the fluorescence recovery of CIZS QDs, thus allowing the system to be activated by GSH. The overexpressed GSH in cancer cells and the NIR region of CIZS QDs enabled the probe for tumor site in situ imaging specifically. Moreover, the Cu-based peroxidase-mimicking catalytic property and Fe^{2+}-triggered Fenton reaction could generate·OH from H_2O_2 allowed the system to realize efficient CDT. Fe^{3+} generated from the Fenton reaction could act as a T_1-weighted MR imaging agent, thus may potentially be used as an effective theranostic tool. Therefore, we simplified the construction of multifunctional system and could simultaneous integration of diagnostic imaging and therapy capability. This work provides new insights into the fluorescence detection of GSH and the simultaneous realization of cancer diagnosis and therapy based on multifunctional nanoplatform.

CRediT authorship contribution statement

Yibing Liu: Conceptualization, Investigation, Data curation, Validation and Writing – original draft preparation. **Xue Jiang:** Data curation, Investigation. **Wei Wang:** Formal analysis and software. **Wei Zhang:** Formal analysis and software. **Pinyi Ma:** Conceptualization, Project administration, Funding acquisition, Data curation, Writing – review & editing and software. **Yibing Huang:** Investigation, Resources, Writing – review and software. **Daqian Song:** Project administration, Funding acquisition, Resources, Supervision, Analyzed the data and participated in the discussion.

Declaration of Competing Interest

The authors declare that they have no known competing financial interests or personal relationships that could have appeared to influence the work reported in this paper.

Data availability

Data will be made available on request.

Appendix A. Supporting information

Supplementary data associated with this article can be found in the online version at doi:10.1016/j.snb.2023.133420.

References

[1] X. Hu, H. Ye, W. Yan, Y. Sun, Factors associated with patient's refusal of recommended cancer surgery: based on surveillance, epidemiology, and end results, Front Public Health 9 (2021), 785602.
[2] T. Wang, Y. Chen, B. Wang, X. Gao, M. Wu, Recent progress in second near-infrared (NIR-II) fluorescence imaging in cancer, Biomolecules 12 (2022) 1044.
[3] S.S. Lucky, K.C. Soo, Y. Zhang, Nanoparticles in photodynamic therapy, Chem. Rev. 115 (2015) 1990–2042.
[4] C. Liang, L. Xu, G. Song, Z. Liu, Emerging nanomedicine approaches fighting tumor metastasis: animal models, metastasis-targeted drug delivery, phototherapy, and immunotherapy, Chem. Soc. Rev. 45 (2016) 6250–6269.
[5] T. Feng, X. Ai, G. An, P. Yang, Y. Zhao, Charge-convertible carbon dots for imaging-guided drug delivery with enhanced in vivo cancer therapeutic efficiency, ACS Nano 10 (2016) 4410–4420.
[6] J. Kim, Y. Piao, T. Hyeon, Multifunctional nanostructured materials for multimodal imaging, and simultaneous imaging and therapy, Chem. Soc. Rev. 38 (2009) 372–390.
[7] D.E. Lee, H. Koo, I.C. Sun, J.H. Ryu, K. Kim, I.C. Kwon, Multifunctional nanoparticles for multimodal imaging and theragnosis, Chem. Soc. Rev. 41 (2012) 2656–2672.
[8] C.S. Cutler, H.M. Hennkens, N. Sisay, S. Huclier-Markai, S.S. Jurisson, Radiometals for combined imaging and therapy, Chem. Rev. 113 (2013) 858–883.
[9] J. Kim, J.E. Lee, S.H. Lee, J.H. Yu, J.H. Lee, T.G. Park, et al., Designed fabrication of a multifunctional polymer nanomedical platform for simultaneous cancer-targeted imaging and magnetically guided drug delivery, Adv. Mater. 20 (2008) 478–483.
[10] M. Jermyn, J. Mercier, K. Aubertin, J. Desroches, K. Urmey, J. Karamchandiani, et al., Highly accurate detection of cancer in situ with intraoperative, label-free, multimodal optical spectroscopy, Cancer Res. 77 (2017) 3942–3950.
[11] W.Q. Hu, M. Fang, H.L. Zhao, S.G. Yan, J.P. Yuan, C.W. Peng, et al., Tumor invasion unit in gastric cancer revealed by QDs-based in situ molecular imaging and multispectral analysis, Biomaterials 35 (2014) 4125–4132.
[12] X. Wu, H. Li, E. Lee, J. Yoon, Sensors for in situ real-time fluorescence imaging of enzymes, Chem 6 (2020) 2893–2901.
[13] M. Luan, M. Shi, W. Pan, N. Li, B. Tang, A gold-selenium-bonded nanoprobe for real-time in situ imaging of the upstream and downstream relationship between uPA and MMP-9 in cancer cells, Chem. Commun. 55 (2019) 5817–5820.
[14] M. Tozaki, S. Nakamura, D. Kitagawa, T. Iwase, R. Horii, F. Akiyama, et al., Ductal carcinoma in situ detected during prospective MR imaging screening of a woman with a BRCA2 mutation: the first case report in Japan, Magn. Reson Med Sci. 16 (2017) 265–269.
[15] R. Liu, S. Zhang, T.T. Zheng, Y.R. Chen, J.T. Wu, Z.S. Wu, Intracellular nonenzymatic in situ growth of three-dimensional DNA nanostructures for imaging specific biomolecules in living cells, ACS Nano 14 (2020) 9572–9584.
[16] X.D. Xu, H. Cheng, W.H. Chen, S.X. Cheng, R.X. Zhuo, X.Z. Zhang, In situ recognition of cell-surface glycans and targeted imaging of cancer cells, Sci. Rep. 3 (2013) 2679.
[17] S.A. Jansen, S.D. Conzen, X. Fan, T. Krausz, M. Zamora, S. Foxley, et al., Detection of in situ mammary cancer in a transgenic mouse model: in vitro and in vivo MRI studies demonstrate histopathologic correlation, Phys. Med Biol. 53 (2008) 5481–5493.
[18] H. Kobayashi, M. Ogawa, R. Alford, P.L. Choyke, Y. Urano, New strategies for fluorescent probe design in medical diagnostic imaging, Chem. Rev. 110 (2010) 2620–2640.
[19] R.G. Aswathy, Y. Yoshida, T. Maekawa, D.S. Kumar, Near-infrared quantum dots for deep tissue imaging, Anal. Bioanal. Chem. 397 (2010) 1417–1435.
[20] H. Zhong, Y.X. Wu, S. Yu, X. Wang, K. He, D. Li, et al., Two-photon CQDs-based dual-mode nanoprobe for fluorescence imaging and magnetic resonance imaging of intracellular wide pH, Anal. Chem. 93 (2021) 5691–5699.
[21] C. Guo, M. Xu, S. Xu, L. Wang, Multifunctional nanoprobes for both fluorescence and (19)F magnetic resonance imaging, Nanoscale 9 (2017) 7163–7168.
[22] J. Cui, R. Jiang, C. Guo, X. Bai, S. Xu, L. Wang, Fluorine grafted Cu_7S_4-Au heterodimers for multimodal imaging guided photothermal therapy with high penetration depth, J. Am. Chem. Soc. 140 (2018) 5890–5894.
[23] J. Sheng, X. Jiang, L. Wang, M. Yang, Y.N. Liu, Biomimetic mineralization guided one-pot preparation of gold clusters anchored two-dimensional MnO_2 nanosheets for fluorometric/magnetic bimodal sensing, Anal. Chem. 90 (2018) 2926–2932.
[24] Z. Zhao, H. Fan, G. Zhou, H. Bai, H. Liang, R. Wang, et al., Activatable fluorescence/MRI bimodal platform for tumor cell imaging via MnO_2 nanosheet-aptamer nanoprobe, J. Am. Chem. Soc. 136 (2014) 11220–11223.
[25] M.J. Allalunis-Turner, R.S. Day 3rd, J.D. McKean, K.C. Petruk, P.B. Allen, K. E. Aronyk, et al., Glutathione levels and chemosensitizing effects of buthionine sulfoximine in human malignant glioma cells, J. Neurooncol 11 (1991) 157–164.
[26] B.R. Stockwell, J.P. Friedmann Angeli, H. Bayir, A.I. Bush, M. Conrad, S.J. Dixon, et al., Ferroptosis: a regulated cell death nexus linking metabolism, redox biology, and disease, Cell 171 (2017) 273–285.
[27] X. Zhang, X. Chen, Y.W. Jiang, N. Ma, L.Y. Xia, X. Cheng, et al., Glutathione-depleting gold nanoclusters for enhanced cancer radiotherapy through synergistic external and internal regulations, ACS Appl. Mater. Interfaces 10 (2018) 10601–10606.
[28] X. Zhang, F.G. Wu, P. Liu, N. Gu, Z. Chen, Enhanced fluorescence of gold nanoclusters composed of $HAuCl_4$ and histidine by glutathione: glutathione detection and selective cancer cell imaging, Small 10 (2014) 5170–5177.
[29] J. Chen, H. Meng, Y. Tian, R. Yang, D. Du, Z. Li, et al., Recent advances in functionalized MnO_2 nanosheets for biosensing and biomedicine applications, Nanoscale Horiz. 4 (2019) 321–338.
[30] J. Chen, Z. Huang, H. Meng, L. Zhang, D. Ji, J. Liu, et al., A facile fluorescence lateral flow biosensor for glutathione detection based on quantum dots-MnO_2 nanocomposites, Sens Actuators B Chem. 260 (2018) 770–777.
[31] Q.Y. Cai, J. Li, J. Ge, L. Zhang, Y.L. Hu, Z.H. Li, et al., A rapid fluorescence "switch-on" assay for glutathione detection by using carbon dots-MnO_2 nanocomposites, Biosens. Bioelectron. 72 (2015) 31–36.
[32] W. Guo, N. Chen, C. Dong, Y. Tu, J. Chang, B. Zhang, One-pot synthesis of hydrophilic ZnCuInS/ZnS quantum dots for in vivo imaging, RSC Adv. 3 (2013) 9470–9475.
[33] M. Jiao, Y. Li, Y. Jia, Z. Yang, X. Luo, Aqueously synthesized color-tunable quaternary Cu-In-Zn-S quantum dots for Cu(II) detection via mild and rapid cation exchange, Sens Actuators B Chem. 294 (2019) 32–39.

[34] B. Zhang, Y. Wang, C. Yang, S. Hu, Y. Gao, Y. Zhang, et al., The composition effect on the optical properties of aqueous synthesized Cu-In-S and Zn-Cu-In-S quantum dot nanocrystals, Phys. Chem. Chem. Phys. 17 (2015) 25133–25141.

[35] X.P. Zhang, C.X. Zhao, Y. Shu, J.H. Wang, Gold nanoclusters/iron oxyhydroxide platform for ultrasensitive detection of butyrylcholinesterase, Anal. Chem. 91 (2019) 15866–15872.

[36] W. Song, X.P. Zhang, B. Lin, Y. Shu, J.H. Wang, Sensitivity dependence on the crystal forms of a fluorescence quencher for silicon quantum dots and its use in acetylcholinesterase assay, Anal. Chem. 93 (2021) 14900–14906.

[37] H. Wang, C.H. Xu, W. Zhao, H.Y. Chen, J.J. Xu, Alkaline phosphatase-triggered etching of Au@FeOOH nanoparticles for enzyme level assay under dark-field microscopy, Anal. Chem. 93 (2021) 10727–10734.

[38] Y. Cao, J. Liu, L. Zou, B. Ye, G. Li, Ratiometric fluorescence sensing of glutathione by using the oxidase-mimicking activity of MnO_2 nanosheet, Anal. Chim. Acta 1145 (2021) 46–51.

[39] H.S. Jung, X. Chen, J.S. Kim, J. Yoon, Recent progress in luminescent and colorimetric chemosensors for detection of thiols, Chem. Soc. Rev. 42 (2013) 6019–6031.

[40] G. Huang, R. Liu, Y. Hu, S.-H. Li, Y. Wu, Y. Qiu, et al., FeOOH-loaded mesoporous silica nanoparticles as a theranostic platform with pH-responsive MRI contrast enhancement and drug release, Science China, Chemistry 61 (2018) 806–811.

Yibing Liu is currently a graduate student in College of Chemistry, Jilin University. Her interest is spectral analysis.

Xue Jiang is currently a graduate student in College of Life Sciences, Jilin University. Her interest is antimicrobial peptide synthesis.

Wei Wang is currently a graduate student in College of Chemistry, Jilin University. Her interest is spectral analysis.

Wei Zhang is currently a graduate student in College of Chemistry, Jilin University. Her interest is spectral analysis.

Pinyi Ma gained his doctor's degree from College of Chemistry, Jilin University in 2017 and he is a engineer in that school. His research area is spectral analysis.

Yibing Huang gained his doctor's degree from College of Life Sciences, Jilin University in 2003 and he is an associate professor in that school. His research areas is modification and self-assembly of peptides, drug slow release.

Daqian Song gained his doctor's degree from College of Chemistry, Jilin University in 2003 and he is a professor in that school. His research areas are spectral and chromatography analysis.